Magnetic-field coils for metastability-exchange optical pumping, spectroscopy, and magnetic resonance of helium

Pierre-Jean Nacher

Laboratoire Kastler Brossel — Physique quantique et applications
Accepted manuscript, published Aug. 22, 2024 in *Rev. Sci. Instrum.*, **95**, 083306, doi: 10.1063/5.0216482

Magnetic-field coils for metastability-exchange optical pumping, spectroscopy, and magnetic resonance of helium

Pierre-Jean Nacher*

Laboratoire Kastler Brossel, ENS-Université PSL, CNRS, Sorbonne Université, Collège de France; 24 rue Lhomond, 75005 Paris, France.

Abstract Optical pumping on the 2^3S–2^3P transition (1083 nm) of metastable ^{3}He or ^{4}He atoms is used for science and applications. Gas is usually enclosed in elongated cells with lengths ranging from several centimeters to several meters for efficient absorption. Good magnetic-field homogeneity is needed for weak diffusion-induced relaxation and long nuclear magnetic resonance signal lifetimes. A compact coil system is designed using a target-oriented numerical optimisation method. It provides a suitably uniform field over cell volumes, with characteristics depending on the chosen optimisation parameters. Additional pairs of coils can be used to generate transverse field components with contributions to the total field inhomogeneities that are discussed.

1 Introduction

Optical pumping (OP) operating on the 2^3S metastable state of helium is an efficient method used to achieve high polarisations in low-pressure helium gas. In ^{3}He or isotopic mixtures of ^{3}He and ^{4}He, it yields high nuclear polarisations in the ^{3}He ground state via metastability-exchange (ME) collisions, and MEOP is used for a variety of applications.[1] Weak rf discharges are used to sustain a suitable density of metastable atoms, with typical absorption lengths as long as meters, especially at high polarisations. Therefore, long cells or sets of parallel long cells are used to significantly absorb the available laser pumping light and polarise large volumes of gas, that is subsequently compressed by high-yield polarisation-preserving compressors.[2] More compact polarising systems can be designed with shorter OP cells, with smaller volumes better suited to smaller-scale compressors.[3, 4, 5, 6] In all systems, the polarised gas is compressed into a storage volume situated in the vicinity of the OP cell or cells.

A holding magnetic field **B** must be applied along the direction of propagation of the circularly-polarised light beam used for OP. A field magnitude of the order of 1 mT or less is generally used, with a high enough relative homogeneity so as to avoid fast gradient-induced magnetic relaxation of the (longitudinal) nuclear polarisation. The rate of this relaxation can usually be linked to the gradients of the transverse field components B_x and B_y and depends on gas pressure.[7] The average relaxation rate over an extended volume, in which field inhomogeneities may significantly differ from linear variations, may be computed from maps of the local values of ∇B_x and ∇B_y. Efficient operation of gas polarising systems requires negligible relaxation-induced losses both in the OP cell, in which the low-pressure (∼mbar) gas dwell time is usually of the order of tens to hundreds of seconds, and in the storage volume, in which high-pressure (∼bar) gas may reside for tens to hundreds of minutes. This is typically achieved for relative field inhomogeneities below a few 10^{-3}/cm in the relevant volumes (see Sect. 2.2 for the evaluation of the targeted inhomogeneities). In addition, monitoring of the gas magnetisation in the storage volume by pulsed nuclear magnetic resonance (NMR) is usually implemented. Long coherence times (T_2^*) of NMR precession, needed for sensitive measurements, require a high absolute homogeneity of the longitudinal field component B_z, typically better than 100 nT over the storage volume.

Various designs have been described to generate holding fields **B** with suitable homogeneity. Large enough Helmholtz coils[3] or sets of four circular coils (two pairs with different diameters),[6] providing highly uniform fields over spherical volumes, are used in some compact systems. Larger numbers of circular coils or end-compensated solenoids, sometimes combined with magnetic shields, are used for MEOP of very long cells.[2] This article reports on the design and performance of systems of coils providing fields with sufficient uniformity over cylindrical OP cells of intermediate lengths (typically up to 60 cm) and diameters up to 6 cm while retaining as small a footprint as possible. Geometrical constraints and ease of construction are met with coil systems comprising six square coils wound on identical frames, an extension of the schemes of Merritt et al.[8] However, in contrast with usual coil design approaches, performing exact field calculations is preferred here to using Taylor expansions of the field components. Numerical optimisation of coil parameters is performed to minimise suitable cost functions related to necessary field homogeneity over OP and storage volumes. This approach is shown to yield significantly better solutions than the cancellation of low-order field derivatives at the origin which is often used.[8, 9, 10, 11]

This article is organised as follows: Sect. 2 introduces notations to describe the coil systems and perform numerical field computations, then describes the method used for optimisations of field maps. Sect. 3 first describes re-

*nacher@lkb.ens.fr, corresponding author.

sults for simple on-axis optimisation, then for joint optimisations over OP and storage volumes, and additionally discusses the effect of simple Earth's field compensation coils. Illustrative comparisons with selected characteristics of experimental systems are given. Key results and possible extensions are briefly discussed in Sect. 4

2 Coil design

2.1 Field map computations

The building block of the field map computations is the integrated Biot–Savart law for a straight current path element. With the notations in Fig. 1a, the field at point P from the current I flowing from P_1 to P_2 is perpendicular to the plane of the figure and its magnitude is

$$B_{12} = \frac{\mu_0 N I}{4\pi r_\perp} \left(\sin\alpha_2 - \sin\alpha_1\right). \tag{1}$$

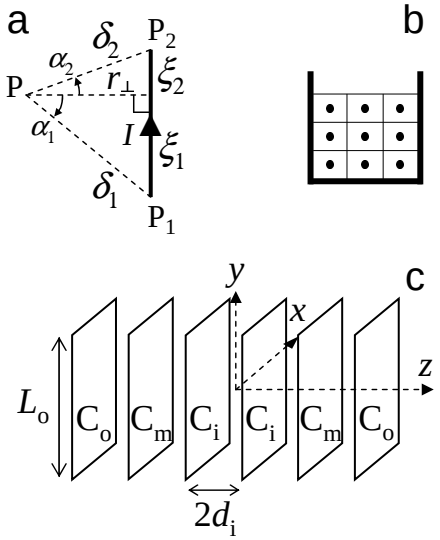

Figure 1: Schematics of current elements generating the magnetic field. a: Geometrical parameters for computing the field magnitude at point P from the current path $P_1 \rightarrow P_2$ (Eq. 1). b: Approximation of an extended winding partly filling a rectangular U-profile, replaced with a lattice of linear currents (here 3×3 elements). c: Three pairs of square coils (inner, median, and outer, C_i, C_m, and C_o) are symmetrically placed along the z-axis. Their side lengths (L), separations ($2d$), and numbers of turns (N, not displayed), carry the index i, m, or o designating the relevant coil pair.

This elementary field magnitude can be expressed in terms of the distances δ_j between P and P_j, ξ_1, ξ_2 and $L = \xi_1 + \xi_2$ between P_1 and P_2 (see Fig. 1a) as

$$B_{12} = \frac{\mu_0 N I}{4\pi} \left(\frac{\xi_1}{\delta_1} - \frac{\xi_2}{\delta_2}\right) \left(\delta_1^2 - \xi_1^2\right)^{-1/2}, \tag{2}$$

where the various lengths can be computed from the coordinates of P (x, y, z) and of P_j $(x_j, y_j, z_j;\ j = 1, 2)$:

$$\delta_j = \left[(x_j - x)^2 + (y_j - y)^2 + (z_j - z)^2\right]^{-1/2} \tag{3}$$

$$\xi_j = \left[(x - x_j)(x_2 - x_1) + (y - y_j)(y_2 - y_1) + (z - z_j)(z_2 - z_1)\right]/L. \tag{4}$$

The lengths ξ_j are evaluated from the dot products $\overrightarrow{P_jP}.\overrightarrow{P_1P_2}$ whereas the direction of the field is that of the cross product $\mathbf{\Lambda} = \overrightarrow{P_1P} \times \overrightarrow{P_1P_2}$, with components:

$$\Lambda_x = (z_2 - z_1)(y - y_1) - (y_2 - y_1)(z - z_1), \tag{5}$$

$$\Lambda_y = (x_2 - x_1)(z - z_1) - (z_2 - z_1)(x - x_1), \tag{6}$$

$$\Lambda_z = (y_2 - y_1)(x - x_1) - (x_2 - x_1)(y - y_1). \tag{7}$$

The components of the magnetic field can finally be expressed from those of $\mathbf{\Lambda}$ using

$$\mathbf{B}_{12} = B_{12}\mathbf{\Lambda}\left(\Lambda_x^2 + \Lambda_y^2 + \Lambda_z^2\right)^{-1/2}. \tag{8}$$

Equations 2 to 8 are explicitly used in computer codes to numerically evaluate the magnetic field components B_x, B_y, and B_z at any point P.

Typical coils comprise tens to hundreds of turns of wire with a circular cross section layered inside U-shaped profiles. The detailed distribution of current density in the coil cross-section is not evaluated and the helical winding pattern is overlooked;[11] instead the field generated by a discrete lattice of $n \times p$ elementary currents inside the winding volume (Fig. 1b) is computed. In practice, n and p range from 1 for a fast coarse approximation to 10 for the most accurate computations.

The coil sets consist of three pairs of square coils arranged as sketched in Fig. 1c. The components of the total field at point P are computed by summing the $24np$ contributions obtained using Eq. 8 for the elementary currents representing each side of each coil. Their expressions involve the common inner side length $L_{\min}$ of the frames, the widths and thicknesses of the windings, the coil spacings, and the number of turns (all coils are connected in series). This summation is numerically performed as well. The typical computation time of one field value is of the order of 1 μs for $np = 1$ using a standard PC (Intel i7 CPU at 4 GHz, GNU Fortran compiler, –O3 optimisation for speed).

2.2 Optimisation of coil parameters

Six parameters are used to characterise the coil system configurations: the three coil half-separations d_k and the three numbers of turns N_k. As a coarse approximation, only two ratios of turns, e.g. N_i/N_o and N_m/N_o, may strongly influence the field maps and are, therefore, retained as free parameters for the optimisations besides the values of d_k. However, since all N_k are integers in actual systems, the value of N_o is indeed relevant. Moreover, coil

construction details such as the widths and depths of the windings also influence the field maps.

As discussed in the introduction, the optimised field map should jointly achieve high uniformity of all its components over the volume V_S of a storage cell (typically a sphere) and of its transverse components over the volume V_{OP} of the OP cell (long cylinders). The locations of these volumes are sketched in Fig. 2 for two examples of coil systems actually implemented in gas polarising systems (Fig. 3). The construction,, operation, and performance of these polarising systems will be described elsewhere, but selected characterisations of their field homogeneity are reported in Sect. 3.

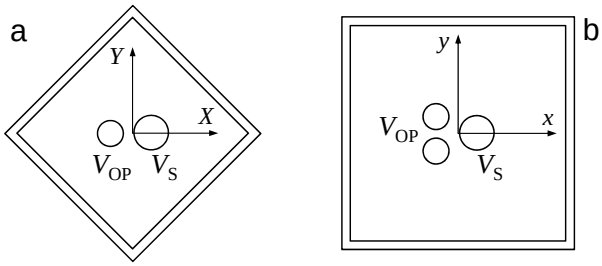

Figure 2: Views in the plane $z = 0$ of the locations of the spherical storage cell V_S and the cylindrical OP cell(s) V_{OP} for two coil sets. a: For the smaller set ($L_{min} = 38.4$ cm) the cells are offset from the coil set center along a diagonal direction X: -5.5 cm for V_{OP} (I.D. 4.5 cm, length 50 cm) and 4.5 cm for V_S (I.D. 8 cm) b: For the larger set ($L_{min} = 50.4$ cm) the OP volume comprises two cylinders (offsets -5.2 cm and ± 4 cm, I.D. 6.1 cm, length 65 cm); V_S offset: 4 cm.

Cost functions defined from computed field maps are used to assess the field uniformity over each volume that is relevant to the targeted application. For the OP volume V_{OP}, two averages over V_{OP} are considered, both scaled to the squared value B_c^2 of the field at the coil center:

$$F_1 = B_c^{-2} \left\langle \nabla B_x^2 + \nabla B_y^2 \right\rangle_{V_{OP}} \tag{9}$$

$$F_1' = B_c^{-2} \left\langle (\partial B_z/\partial z)^2 \right\rangle_{V_{OP}} \tag{10}$$

F_1 combines the squared gradients of the transverse components of $\mathbf{B}$ that are involved in the computation of the longitudinal relaxation rate $1/T_1$:[7]

$$1/T_1 = DF_1, \tag{11}$$

where D is the diffusion coefficient that depends on gas pressure p as $Dp = 0.1914(T/300)^{1.71}$ mbar×m^2/s (T is the gas temperature in K).[5] In contrast, F_1' averages squared derivatives with respect to z in Eq. 10, and only those of B_z that are not directly relevant for relaxation. However all components and their variations are linked by Maxwell's Equations and F_1' is expected to be a relevant indicator for the minimisation of $1/T_1$ in V_{OP}, at least for axisymmetric configurations. In practice, the averages in

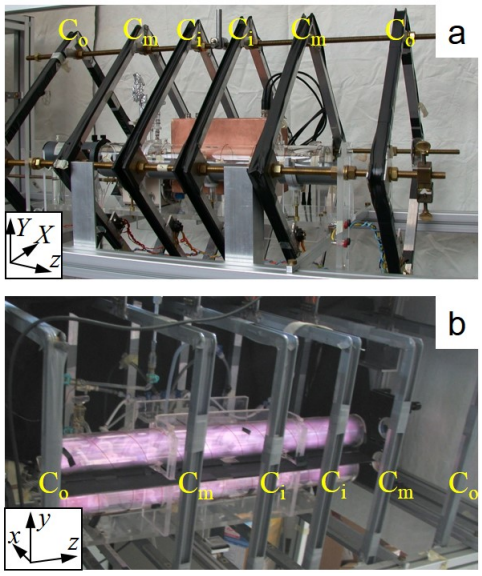

Figure 3: Side views of assembled sets of coils comprising six square coils in aluminum frames labelled according to Fig. 1c, containing OP cells consisting of a single (a) or a double (b) glass cylindrical volume. The RF discharge used for MEOP is active in Fig. b only.

Eqs. 9 or 10 are performed by computing $\mathbf{B}$-values at 50 z-locations regularly spaced on half of the axis of V_{OP} ($z \geq 0$). The volume average for F_1 is evaluated from values every cm in the transverse directions whereas that of F_1' only uses finite differences between adjacent z-locations on the axis of V_{OP}, which makes its computation much faster than that of all derivatives on a 3D grid.

For the low gas pressures relevant in MEOP, fast gas diffusion within V_{OP} enforces a uniform gas polarisation, and $1/T_1$ is the volume average of local values of $1/T_1(z)$ that are involved in Eq. 9. In the storage volume V_S, the higher gas pressures automatically yields decreased diffusion and reduced relaxation rates of the uniform polarisation (Eq. 11), a rate usually slow enough for the targeted application. A different contribution to the cost function is therefore introduced: the volume average of the squared deviation of B_z from its average $\overline{B_z}$, also scaled to B_c^2 :

$$F_2 = B_c^{-2} \left\langle \left(B_z - \overline{B_z}\right)^2 \right\rangle_{V_S}. \tag{12}$$

F_2 quantifies the width of the distribution of Larmor frequencies during NMR precession and is therefore directly related to the signal half-life T_2^* involved in the signal-to-noise ratio of NMR measurements.[12] In practice, the average in Eq. 12 is computed over 1/4 of the spherical volume on a grid comprising 11 points along a diameter of V_S ($z \geq 0$ and Y or $y \geq 0$, 172 sites).

The optimisation of the coil parameters is achieved by minimisation of a cost function combining F_1 or F_1' and

F_2:

$$F = (F_1 + f_{21}F_2 + F_{\rm add})^{1/2}, \quad (13)$$

$$F' = (F_1' + f_{21}F_2 + F_{\rm add})^{1/2} \quad (14)$$

where f_{21} is a parameter used to control the balance in required field homogeneity between OP and storage volumes, and $F_{\rm add}$ introduces additional terms that increase rapidly when targeted geometrical constraints are not met (the coils should not overlap, $d_{\rm o}$ should not exceed a set value, ...). The minimisation of the total cost function F or F' is numerically achieved using the robust downhill simplex method [13] implemented in the amoeba routine of Ref.[14] As is usual in minimisation protocols, the choice of a suitable initial set of parameters and their probed variations (here, 20%) is important to avoid possible local minima and efficiently reach the solution. Attempts from different starting points and restarts from end points are used to ensure good convergence. Successive steps are actually performed to accelerate convergence to an optimal configuration.

As the first step, a coarse approximation of the windings by single current loops ($n = p = 1$) is made. Aluminum alloy frames made from welded U-profile ($20\times20\times20\times2$ mm^4) are used for the sets of coils in Fig. 3. The windings within these frames are arranged in 1-mm-thick layers of 16 turns with a maximum of 16 layers to fill the winding volume. The same wire gauge and winding parameters are assumed for computations of six-coil sets throughout this article. A number of turns of $N_{\rm o} = 224$ (14 layers) for the outer pair of coils is chosen at this stage since it approximately fills 90% of the winding volume. The minimisation of F or F' is performed for chosen geometrical constraints (size of coils, size and positions of volumes $V_{\rm OP}$ and $V_{\rm S}$) and for a fixed value of f_{21} in Eq. 13 or 14. The corresponding optimal set of parameters (d_i and N_i) is used to compute illustrative 2D field maps and to evaluate the values of T_1 in $V_{\rm OP}$ and T_2^* in $V_{\rm S}$. The full expression F_1 of Eq. 9 is used to evaluate T_1 even when F' is used for the optimisation. Visual inspection of the field maps is used to qualitatively assess the field homogeneity, while the comparison of the relaxation rates with targeted upper bounds for these rates is used to choose the weight f_{21} given to field inhomogeneities over $V_{\rm S}$ in the minimised function F or F', as shown in an example in Section 3.2. At the end of the process, it can be concluded whether a configuration with coils of a set size ($L_{\rm min}$, maximum $d_{\rm o}$) can yield satisfactory field homogeneity over the chosen OP and storage volumes.

The second optimisation step consists of replacing the single current loops with discrete lattices of currents (Fig. 1b) and therefore computing more realistic field maps, optimal coil positions, and ratios of numbers of turns ($N_{\rm i}/N_{\rm o}$, $N_{\rm m}/N_{\rm o}$).

The third step consists of finding three integer numbers of turns with ratios closely approximating the optimal ratios found in the second step, and performing the optimisation of the three coil positions for these fixed numbers of turns. This set of parameters is used for the construction of the coil frames, and the actual dimensions of the coil windings are used for a final optimisation of the coil positions. Small variations of geometric parameters can also be used at this stage to probe the sensitivity of field maps to construction or winding imperfections. For instance, variations in one coil pair spacing d_k by ±2 mm typically shorten T_1 by less than 10%.

3 Results

3.1 On-axis optimisation

The results displayed in Fig. 4 illustrate the differences in optimal parameters and resulting field maps for similar coil systems designed using the target-oriented numerical optimisation reported in this article or using an analytical method.[10]

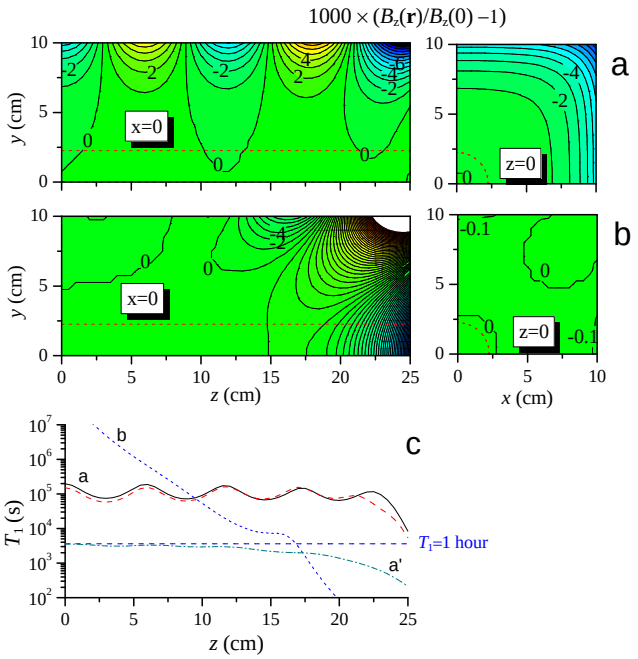

Figure 4: Computed field maps (a and b) and associated relaxation times (c) for sets of six square coils of equal side lengths $L = 0.4$ m, with positions and numbers of turns listed in Table 1. Maps and curves a: results of on-axis optimisation over an extended cell volume. b: results for the analytically derived coil parameters of Ref. [10] The maps of $B_z(\mathbf{r})/B_z(0) - 1$ are displayed in one quadrant of vertical planes (with contours every 0.1%). The dashed lines in the maps mark the on-axis location of $V_{\rm OP}$. c: computed variations of local T_1 with z for ^{3}He gas at $p = 0.4$ mbar. Curves a are obtained for maps minimising F_1 (solid black line) or F_1' (dashed red line). Curve a′ is the local T_1 (in field map a) for the off-axis OP volume in Fig. 2a. Curve b is the on-axis local T_1 for the field map of Ref. [10]

Here, in contrast with coil systems designed to ac-

commodate an OP cell and a storage cell (Fig. 2 and Refs.[4, 5]), the coil parameters are varied to only minimise F_1 over an OP cell centred on the z-axis. This solution can be of interest for various applications, and can be directly compared to that proposed in Ref. [10] More precisely, the 'wire coils' parameters in Table 1 and the maps in Fig. 4a are obtained for sets of current loops having the same side length as those of Ref. [10] The optimal ratios

system	d_i, d_m, d_o (cm)	N_i, N_m, N_o (turns)	$B_z(0)/I$ (mT/A)
Wire coils	6.03, 18.50, 35.41	84, 93, 189	0.825
Real coils	5.93, 18.14, 34.96	87, 95, 204	0.877
Ref. [10]	3.66, 12.20, 27.34	57, 78, 200	0.888

Table 1: Optimised coil positions, number of turns, and computed field at coil centre for three configurations of coil sets. The first two lines minimise F_1 (Eq. 9) for a 25-cm-long cell centred on the z-axis, for single current loops (Wire coils) or realistic extended windings (Real coils). The Wire coils system is given for direct comparison with the coil system of Ref. [10] (third line).

found in that case ($N_\mathrm{i}/N_\mathrm{o} = 0.4447$, $N_\mathrm{m}/N_\mathrm{o} = 0.4917$) yield minimal rounding errors for $N_\mathrm{o} = 189$ and the final parameters in the first line of Table 1. The field maps of the two systems plotted in Figs. 4a and 4b exhibit features associated with their optimisation approaches: field deviations within 10 cm from the coil centre are much weaker in Fig. 4b (note that contour lines are drawn every 10^{-4} for the transverse plane map and every 10^{-3} for the other maps). However, as expected, field deviations remain moderate further away from the coil centre (between $z = 10$ cm and $z = 25$ cm) only in Fig. 4a. As a result, the values of z-dependent magnetic relaxation time in Fig. 4c, computed for a 5-cm-diameter OP cell, remain safely long enough for efficient MEOP over the whole plotted range of z only for the suitably designed system (solid curve labelled a): in that case, T_1 exceeds 1 hour at the lower end of the gas pressure range used for efficient MEOP.[1] The differences in system parameters and in the corresponding variations of T_1 with z obtained by minimisation of F_1 or F_1' are very small, as could be expected for an OP volume close to the axis of symmetry of the system. Figure 4c also displays the variation of T_1 in an off-axis OP volume. All variations of T_1 correlate well with the displayed field maps.

The smaller of the sets of six square coils used in gas polarising systems (Fig. 2a) has an average side length of order 0.4 m, the same as that of the coil systems compared in Fig. 4. The second optimisation step starting from the wire coil solution in Table 1 is, therefore, performed for realistic winding sizes, yielding the configuration given for 'Real coils' in Table 1. The optimal coil positions are only slightly affected, but larger modifications in the numbers of turns (in the ratios $N_\mathrm{i}/N_\mathrm{o} = 0.4265$ and $N_\mathrm{m}/N_\mathrm{o} = 0.4657$) are found with respect to the optimised wire coils. However, the differences (not shown) in field maps and in z-dependent relaxation times are very small. An alternative solution for $N_\mathrm{o} = 176$ also yields very similar field and T_1 maps.

3.2 Off-axis optimisation

For gas polarising systems, the joint optimisation of field maps over the off-axis OP and storage volumes instead of the on-axis optimisation achieved in Section 3.1 starts with a series of coarse calculations: the first minimisation step mentioned at the end of Sect. 2.2, with $n = p = 1$ and non-integer numbers of turns. For fixed coil size as well as OP and storage volumes and locations, the influence of the choice of the parameter f_{21} in Eq. 9 or 10 on the performance of the optimised coil system is first assessed. Figure 5 displays the corresponding results for the relaxation time T_1 in the OP cell and the NMR decoherence time T_2^* in the storage volume of the larger coil system (Fig. 2b). In addition, the outcomes of minimisations based on the use of F or F' are compared (solid or open symbols, respectively). With both approaches, joint decreases in T_1 and increases in T_2^* with f_{21} are found, but the use of F' for computations which are typically ten times faster should not be trusted to yield reliably optimised configurations for off-axis OP and storage volumes. Figure 5 also indicates that choosing f_{21} of the order of 1 yields satisfactory values $T_1 \approx 1700$ s and $T_2^* \approx 3$ s for this coil system. The same study for the smaller coil system in Fig. 2a yields similar variations of T_1 and T_2^* with f_{21}, but with values typically 1.5–2.5 times shorter than those obtained for the larger system.

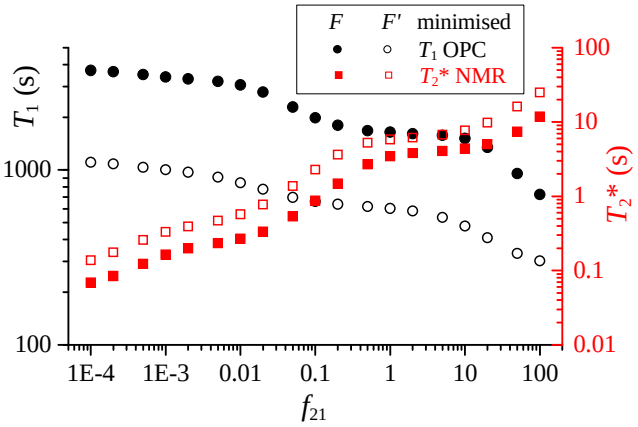

Figure 5: Computed global T_1 in V_OP (for $p = 0.4$ mbar) and T_2^* in V_S (for a Larmor frequency of 40 kHz, typical of actual systems) obtained for the system in Fig. 2b when minimising F or F' (see the legend). The parameter f_{21} sets the relative weight of inhomogeneities in the minimisation process (Eqs. 13 and 14).

The next optimisation steps for the two configurations in Fig. 2 yields parameters and associated field maps that significantly differ from the results of on-axis optimisations. Sets of optimised parameters are listed in Table 2

(for arbitrary numbers of turns) and the first part of Table 3 (for integer numbers of turns, sets a and b), corresponding to minimisations of the cost function F of Eq. 13 with $f_{21} = 1$.

set	$L_{\min}$ (cm)	d_i, d_m, d_o (cm)	$N_\mathrm{i}/N_\mathrm{o}$, $N_\mathrm{m}/N_\mathrm{o}$	$1/T_1$ (h^{-1})
a	38.4	4.90, 16.47, 33.26	0.3661, 0.4825	5.38
b	50.4	6.52, 21.88, 43.75	0.3767, 0.4894	2.17

Table 2: Optimised coil positions, ratios of numbers of turns, and averaged relaxation rates in V_OP for $p = 0.4$ mbar (the corresponding averaged relative gradients from Eq. 11 are 5.6×10^{-4} and 3.6×10^{-4} cm^{-1} for sets a and b). Results are obtained by minimising the cost function F for the coil sets in Fig. 2 assuming $N_\mathrm{o} = 224$.

Corresponding maps of field inhomogeneities are displayed in Figs. 6a and b, onto which the off-axis locations of the relevant volumes for the optimisations are marked. The z-dependent local T_1 values in the OP volumes are

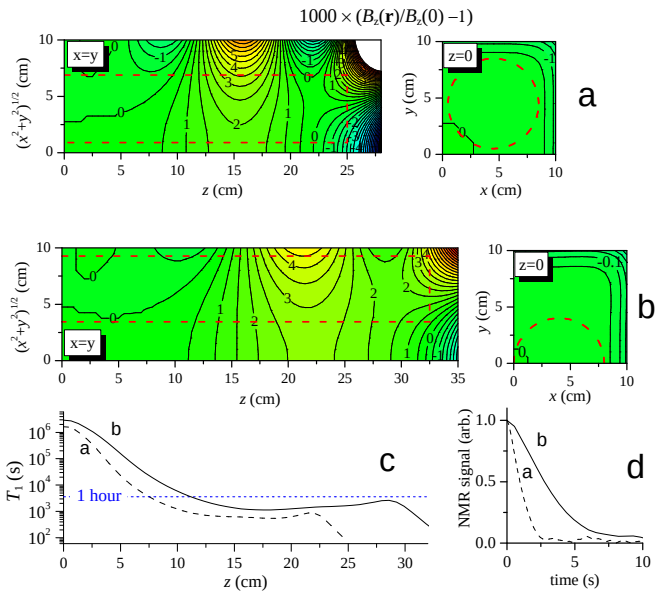

Figure 6: Computed field maps for the smaller (a) and larger (b) sets of coils in Table 3, with contour lines every 0.1% (0.01% in the plane $z = 0$ of b). The dashed lines in the maps mark the locations of V_OP in the diagonal planes $x = y$ and of V_S in the planes $z = 0$. c: Variations of local T_1 in V_OP for $p = 0.4$ mbar. d: NMR signal decays in V_S at 40 kHz.

displayed in Fig. 6c. The computed decoherence of precessing magnetisation within V_S (Fig. 6d) yields signal half-lives of the order of 1 and 3 s .

The second part in Table 3 (sets a′ and b′) lists the parameters used for the construction of the experimental systems depicted in Fig. 3. They were obtained by minimising the cost function F' of Eq. 14, before the quantitative comparison summarised in Fig. 5 was performed,

set	$L_{\min}$ (cm)	d_i, d_m, d_o (cm)	N_i, N_m, N_o (turns)	$B_z(0)/I$ (mT/A)
a	38.4	4.90, 16.47, 33.25	82, 108, 224	0.973
b	50.4	6.54, 21.94, 43.83	90, 117, 239	0.798
a′	38.4	5.90, 19.10, 37.80	85, 100, 224	0.852
b′	50.4	6.17, 20.08, 40.74	80, 101, 221	0.759

Table 3: Sets a and b: Optimised coil positions and numbers of turns for the coil sets in Fig. 2 and computed field values at the coil centre, obtained when minimising the cost function F. The corresponding field maps and data are plotted in Fig. 6. Sets a′ and b′: Parameters obtained when minimising F', used for the experimental systems in Fig. 3. With resistance values of 27 and 37 Ω at room temperature for the coil sets a′ and b′, power dissipation factors of 37 and 67 $\mathrm{W/mT^2}$ are inferred from B/I data.

and therefore the performance of the actual coil systems is expected to be lower than that of the true optimum.

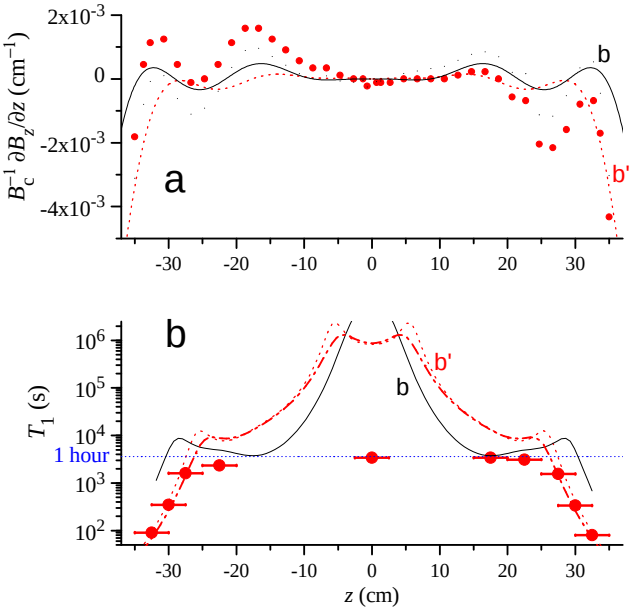

Figure 7: a: Computed axial field derivatives on the OP cell axis for the coil set parameters b and b′ in Table 3 (solid and dotted lines), and corresponding data inferred from B_z measurements for currents $I = \pm 1$ A using a single-axis fluxgate magnetometer (Bartington MAG-01MS, ±1 mT). b: Computed $T_1(z)$ values within V_OP for the coil sets b and b′ ($p = 1.33$ mbar). The dash-dotted line and solid symbols are volume-averaged computed values and experimental results for a 4.5-cm-long (the length of the bars) probing cell (see the text).

This is illustrated in Figs. 7a and b for the larger coil set in Fig. 3b: computed field z-derivatives on the axis of V_OP and local values of T_1 are compared for coil sets b and b′ (solid and dotted lines) and to measured experimental data (solid symbols). The larger than expected oscilla-

tions and the asymmetry of measured data in Fig. 7a are attributed to construction and winding imperfections, but the rapid drop beyond $|z| = 35$ cm which is computed for the b′ coil set is clearly observed.

Experimental T_1 data in Fig. 7b were derived from NMR measurements performed at coil centre using a sealed Pyrex glass cell (I.D. 4.5-cm, length 4.5 cm) filled with 1.33 mbar of MEOP-polarised ^{3}He gas. Free-induction decay (FID) signal ratios for $\pi/4 - \Delta t - \pi/2$ pulse pairs were used for various dwell times Δt spent at different positions z. T_1 values were limited by wall relaxation over most of the explored range of z (1 h is typical for Pyrex glass with such surface-to-volume ratio), and steeply decreased beyond $|z| = 28$ cm, in good agreement with the expected harmonic averages of computed $T_1(z)$ over the length of the probing cell. Computations and experimental checks agree well, and show that performing full optimisation with the more relevant cost function F would have led to a better experimental system, suitable for longer OP volumes with acceptable relaxation losses.

3.3 Control of transverse field components

So far, only the need to apply an axial B_z field has been considered, but transverse field components may play an important role in various situations. For MEOP, the magnetic field applied to optically pumped atoms must be collinear with the circularly polarised OP light beam, and in long cells this can be achieved only if the transverse field components (due, for instance, to the Earth's field $\mathbf{B}^{\mathrm{E}}$) are negligible compared to B_z. Below a few mT this may require compensating these components without introducing significant additional inhomogeneities in the total field $\mathbf{B}$. In other situations, one may wish to deliberately vary the relative orientation of pump or probe light beams with respect to the magnetic field,[15] and it is convenient to operate with fixed orientations of the cell and light beams and use additional sets of coils generating uniform fields along the transverse directions B_x and B_y as well.

Figure 8 shows the full set of coils used in the experiments in Ref. [15] The six square coils, arranged as discussed in Sect. 3.1 or 3.2 depending on the targeted B_z map, are assembled by brass threaded rods near their corners as shown in Fig. 3a. The transverse field components are generated by two pairs of rectangular coils comprising 40 turns each. They are wound inside 20×20 mm^2 PVC wireways assembled using plastic angle brackets. Their outside widths just fit inside the 36-cm clearance of the B_z coils to which they are attached. Their outside lengths are similar to the length of the B_z coil set, with the B_x coil pair fitting inside the longer B_y coil pair. In many locations worldwide the largest of the Earth's field components is vertical, and the z-axis may in addition be coarsely aligned with the Earth's field horizontal component. The required compensating B_y field is therefore usually larger than the compensating B_x field and the longer coil pair, which generates a slightly more uniform field, is used for B_y.

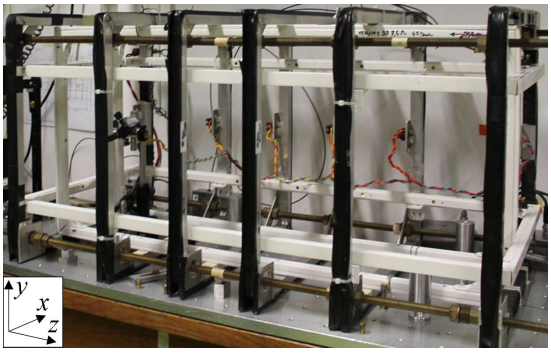

Figure 8: View of an assembled set of magnetic field coils comprising six square coils in aluminum frames (for B_z) and two pairs of rectangular coils in white PVC wireways (for B_x and B_y).

Selected computed field maps of B_y inhomogeneities are displayed in Fig. 9a for average coil positions $d_y = \pm 10$ cm. Note that the typical deviations are one order of magnitude larger than for the six-coil sets (Figs. 4 and 6). The maps of ∇B_x and ∇B_y (relevant for relaxation in the net B_z field) that are due to the compen-

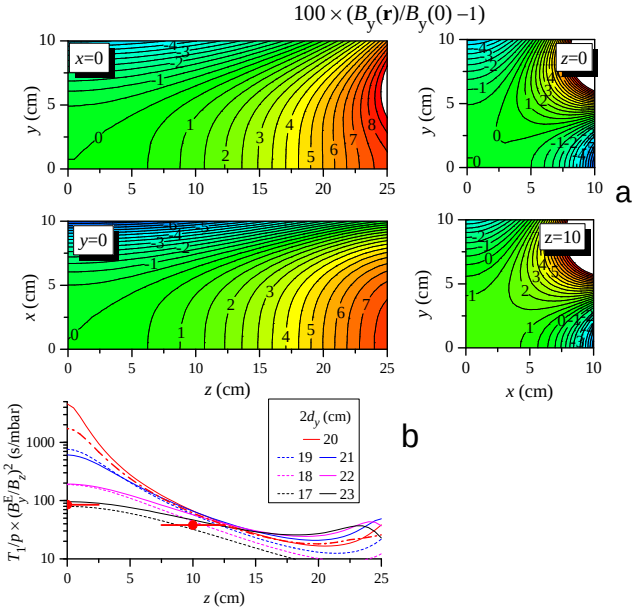

Figure 9: a: Computed field maps for the rectangular B_y coil pair, with side lengths 77 and 34.5 cm and a mean separation of 20 cm. The maps of $B_y(\mathbf{r})/B_y(0) - 1$ are displayed in one quadrant of horizontal and vertical planes including the z-axis and of vertical planes at the coil centre and 10 cm away (contours every 0.5% in all plots). b: Local relaxation times in V_{OP} for $p = 1$ mbar (see the text) for various coil separations of $2d_y$ (see the legend). The dash-dotted line and solid symbols are volume-averaged computed values and experimental results for a 4.5-cm-long (the length of the bars) probing cell and $2d_y = 20$ cm.

sating $-B_y^{\mathrm{E}}$ field are computed and used to infer $T_1(z)$ (Fig. 9b) for a 4.5-cm-diameter OP volume centred on the z-axis. More precisely, T_1 is the product of the displayed data by $(B_z/B_y^{\mathrm{E}})^2$, assuming a negligible contribution to relaxation of the field gradients due to the six-coil set used for B_z. No N-dimensional optimisation is performed to design these compensation coils, and a comparison of the T_1 data computed for different coil separations shows an optimal value of $2d_y = 20$ cm. The field maps of the shorter coil pair used for B_x (72.5-cm-long, not shown) are hardly less uniform and yield similar $T_1(z)$ results. The fields generated by these compensation coils are $B_y = 0.154$ mT/A and $B_x = 0.156$ mT/A. The two data points in Fig. 9b correspond to relaxation in the same cell as inr Fig. 7b. The increase in relaxation rates when $-B_x^{\mathrm{E}} = 15$ μT and $-B_y^{\mathrm{E}} = 34$ μT are applied was measured using optical detection of polarisation at several cell positions for values of B_z ranging from 10 to 200 μT.

4 Discussion

The pragmatic and target-oriented design approach described in this article yields compact coil systems with relative field inhomogeneities at the per mil level over extended and elongated volumes. They are simpler to construct and provide better experimental access than end-compensated solenoids. The typical usable length for OP cells, either on-axis or off-axis, is found to be $\simeq 1.15 \times L$ (the common coil side length), which is 60% longer than is analytically designed similar coil systems (Ref. [10], see Sec. 3.1) while the typical coil set length is $\simeq 1.7 \times L$.

One important parameter characterising the quality of the coil system is the relaxation time T_1 in the OP volume. The variations with z of the local T_1 plotted for various coil systems can be used to assess the dominant location of relaxation losses that may affect MEOP efficiency, and the maximum OP cell dimensions one may use in a given system. For instance, the comparison of Figs. 4c and 6c which correspond to different optimisation objectives (on-axis minimisation of F_1 versus off-axis joint minimisation of F_1 and F_2), illustrates that the sole minimisation of F_1 yields a more uniform $T_1(z)$ both on- and off-axis and therefore a longer overall T_1 (1430 s vs. 670 s). This difference arises from the added constraint on F_2 for Fig. 6c, that is from the higher field uniformity requested at small z in V_{S} which results in poorer uniformity at larger z. In that case, the balance in the values achieved for T_1 and T_2^*, that are both suitable for the targeted application of such coil systems, results from the choice $f_{21} = 1$ made for these optimisations.

With regard to the simple coil pairs of Sect. 3.3 used to control transverse field components, and in particular compensate those of the Earth's field, the influence of their computed inhomogeneities on $T_1(z)$ is found to critically depend both on the operating B_z field value and on the length of V_{OP}. The experimental $T_1(z)$ data induced by field inhomogeneities of these coil pairs are found to be significantly shorter than computed, in contrast to the good agreement obtained for the main field of the six-coil sets. This is attributed to the imprecise positioning of the windings in rather flexible wireways and a more rigid construction is expected to reduce relaxation losses in the vicinity of the coil centre. Further improvement may be obtained using an approach similar to that used for the optimisation of the six-coil sets and computing field maps for optimised sets of two pairs of rectangular coils, instead of one, for each of the transverse directions. Details fall beyond the scope of this article, and the solution was not experimentally tested, but a typical improvement on achievable T_1s by a factor of 10 is obtained for sets of four rectangular coils with the same size as those of the compensating pairs.

More generally, the design method relying on the minimisation of numerically computed cost functions of field maps for sets of coils consisting of straight current elements can be advantageously used in situations where a mere cancellation of coefficients in a Taylor expansion does not offer sufficient control to achieve a specific objective. This approach was for instance found to be efficient in the design of different kinds of low-frequency RF coils used in NMR experiments.[16] Similar approaches involving field computations over an extended volume can be found in the literature, but they use a rather unspecific cost function for a rotationally invariant coil system and field optimisation volume[17] or they involve a simple rms field deviation and very heavy finite element method simulations.[12] Quite generally, defining a suitable cost function specifically tailored to achieving targeted system performance – here, a satisfactory balance of T_1 and T_2^* for gas in different volumes – may be a key step in the design of optimal systems.

Acknowledgments

The contributions of Cavin Talbot and Tangi Baré to the characterisations of experimental systems are gratefully acknowledged.

References

[1] T. R. Gentile, P. J. Nacher, B. Saam, and T. G. Walker. 'Optically polarized ^{3}He.' *Rev. Mod. Phys.*, 89:045004 (2017).

[2] C. Mrozik, O. Endner, C. Hauke, W. Heil, et al. 'Construction of a compact ^{3}He polarizing facility.' *J. Phys. Conf. Ser.*, 294:012007 (2011).

[3] T. R. Gentile, D. R. Rich, A. K. Thompson, W. M. Snow, et al. 'Compressing spin-polarized He-3 with a modified diaphragm pump.' *J. Res. Nat. Inst. Stand. Technol.*, 106(4):709–729 (2001).

[4] J. Choukeife, X. Maitre, G. Tastevin, and P.-J. Nacher. 'On-site production of hyperpolarised helium-3 gas for lung MRI.' In 'Proc. Int. Soc. Magn. Reson. Med.', page 1391 (2003).

[5] G. Tastevin and P.-J. Nacher. 'NMR measurements of hyperpolarized He3 gas diffusion in high porosity silica aerogels.' *J. Chem. Phys.*, 123:064506 (2005).

[6] D. S. Hussey, D. R. Rich, A. S. Belov, X. Tong, et al. 'Polarized He-3 gas compression system using metastability-exchange optical pumping.' *Rev. Sci. Instrum.*, 76(5):053503 (2005).

[7] G. D. Cates, S. R. Schaefer, and W. Happer. 'Relaxation of spins due to field inhomogeneities in gaseous samples at low magnetic fields and low pressures.' *Phys. Rev. A*, 37:2877–2885 (1988).

[8] R. Merritt, C. Purcell, and G. Stroink. 'Uniform magnetic field produced by three, four, and five square coils.' *Rev. Sci. Instrum.*, 54:879–882 (1983).

[9] W. Franzen. 'Generation of uniform magnetic fields by means of air-core coils.' *Rev. Sci. Instrum.*, 33:933 (1962).

[10] W.-Z. Wang, B.-T. Hu, H. Zheng, X.-Q. Tu, et al. 'A new magnetic field system for He-3 polarization.' *Acta Physica Sinica*, 67:176701 (2018).

[11] Y. Huang, L. Jiang, P. Fu, Z. Huang, et al. 'Optimal design method to improve the magnetic field distribution of multiple square coil systems.' *IEEE Access*, 8:171184–171194 (2020).

[12] T. Liu, A. Schnabel, J. Voigt, W. Kilian, et al. 'A built-in coil system attached to the inside walls of a magnetically shielded room for generating an ultra-high magnetic field homogeneity.' *Rev. Sci. Instrum.*, 92(2):024709 (2021).

[13] J. Nelder and R. Mead. 'A simplex method for function minimization.' *The computer journal*, 7(4):308–313 (1965).

[14] W. Press, W. Vetterling, S. Teukolsky, and B. Flannery. *Numerical Recipes in FORTRAN.* Cambridge University Press, London, UK (1988). ISBN 9780521430647.

[15] A. Dia, M. Abboud, P.-J. Nacher, and G. Tastevin. 'Doppler-free spectroscopy of the lowest triplet states of helium using double optical resonance.' *Eur. Phys. J. D*, 75(8):223 (2021).

[16] P.-J. Nacher, S. Kumaragamage, G. Tastevin, and C. Bidinosti. 'A fast MOSFET rf switch for low-field NMR and MRI.' *J. Magn. Reson.*, 310:106638 (2020).

[17] A. E. Krosney, M. Lang, J. J. Weirathmueller, and C. P. Bidinosti. 'Magnetic diffusion, inductive shielding, and the Laplace transform.' *Am. J. Phys*, 89(5):490–499 (2021).